Electrochemical and spectroscopic study of novel Cu and Fe-based catalysts for oxygen reduction in alkaline media

Qinggang He [a,*], Xiaofang Yang [b], Ruihua He [c], Agustín Bueno-López [d], Hamish Miller [e], Xiaoming Ren [f], Wanli Yang [c], Bruce E. Koel [b]

[a] Environmental Energy Technologies Division, Lawrence Berkeley National Laboratory, 1 Cyclotron Road, Berkeley, CA 94720, USA
[b] Department of Chemical and Biological Engineering, Princeton University, Princeton, NJ 08544, USA
[c] ALS, Lawrence Berkeley National Laboratory, 1 Cyclotron Road, Berkeley, CA 94720, USA
[d] Department of Inorganic Chemistry, University of Alicante, Ap. 99 E-03080, Alicante, Spain
[e] Acta SpA, Via di Lavoria, 56/G 56040 Crespina, Pisa, Italy
[f] U. S. Army Research Laboratory, 2800 Powder Mill Rd., RDRL-SED-C, Adelphi, MD 20783, USA

ARTICLE INFO

ABSTRACT

We synthesized two "single-core" $Fe-N_x/C$ and $Cu-N_x/C$ electrocatalysts and a bi-core $CuFe-N_x/C$ composite electrocatalyst using iron and copper phthalocyanine-based precursors and a high-temperature pyrolysis method. The morphology, structure, and activity toward the oxygen reduction reaction (ORR) in alkaline media were evaluated for each electrocatalyst by transmission electron microscopy (TEM), X-ray Diffraction (XRD), and the rotating ring-disk electrode (RRDE) method. Although the $Cu-N_x/C$ catalyst showed lower catalytic activity than $Fe-N_x/C$, the presence of Cu enhanced the ORR performance of bi-core $CuFe-N_x/C$, as compared to single-core $Fe-N_x/C$. To fully understand the synergistic effect between Cu and Fe on this enhancement, high resolution X-ray photoelectron spectroscopy (HR-XPS) and soft X-ray absorption spectroscopy (XAS) was employed to study the electronic structure of as-synthesized electrocatalysts. The HR-XPS analysis showed that metal-nitrogen bonding was maintained and that the oxidation states of Fe and Cu were influenced by the presence of the second metal in the bi-core catalyst. The XAS data revealed that a fraction of an electron was transferred from Fe to Cu, which may help to lower the kinetic barrier during the ORR process. Based on our experimental results and four different models, we briefly discuss ORR mechanisms on these metallic catalysts.

Published by Elsevier B.V.

1. Introduction

Alkaline anion-exchange membrane fuel cells (AEMFC) have intrinsic advantages as compared to their acidic counterparts [1,2]. For example, non-noble (low-cost) electrocatalysts can be employed in both electrodes of an AEMFC; it has improved energy efficiency because of lower anode (fuel) and cathode (air) over-voltages; cathode flooding is less problematic; more-complex fuels may be employed because C–C bond breakage is more facile in alkaline environments; etc ... Among prior and on-going investigations of electrocatalysts for the oxygen reduction reaction (ORR) in high-pH environments, increasing attention has been given to metallomacrocycles as alternatives to Pt and Pt-alloy catalysts

because of cost and supply constraints [3–5]. During preparation of non-noble metal catalysts, a pyrolysis step under inert gas atmosphere is usually necessary to enhance their catalytic activity and stability [6]. Although there is still some debate about the specific processes during high-temperature (600–900 °C) thermal treatment and the formation of the catalytic site [7,8], it is widely accepted that metal-N_x moieties are the active centers for ORR [9,10]. Furthermore, for catalysts derived from pyrolyzed single-core metallomacrocycles, it has been shown that the structure of the molecules undergoes dramatic changes, including contraction of interatomic distances and integration of metal-N_x moieties into the graphitic planes of the carbon support [11,12]. There are also reports about the structure and valence state of dimeric metal catalysts with excellent performance for the ORR [13,14]. Nevertheless, these investigations were limited in macrocles with only a single metallic element. Recently, major progress on metal complex systems reminiscent of enzymes for the ORR [15] was

Table 1
Comparison of CuFe−N$_x$/C, Cu−N$_x$/C, and Fe−N$_x$/C catalysts and their electrode kinetic parameters in 0.1 M KOH at room temperature.

Catalyst	Metal loading (wt.%)	$E_{1/2}$ (V)	Number of exchanged electrons (n)	Mass activity (mA/cm^2 µg catalyst)			Tafel slope	H$_2$O$_2$ yield %	
				@0.90 V	@0.85 V	@0.80 V	(mV/decade)	@0.6 V	@0.7 V
Pt/C	29.7	0.882	4.0	0.158	0.467	1.092	128/75	−	−
CuFe−N$_x$/C	1.7 Cu, 1.5 Fe	0.864	3.96	0.099	0.478	1.513	116/48	6.8	4.0
Cu−N$_x$/C	1.8	0.755	3.55	0.007	0.033	0.116	105/62	33.4	25.7
Fe−N$_x$/C	1.5	0.844	4.0	0.065	0.307	0.972	112/51	2.4	1.3

followed up by a few studies of binary non-noble transition-metal catalysts [16,17]. Both a face-to-face binary metal model [17–19] and a switch-center model [17] were proposed for the ORR process. Central to these proposed models are changes of the local bonding environment and thus the electronic state of the involved metal centers of the binary catalysts with respect to their single-element counterparts. Direct experimental probes to study and confirm such changes, however, remain elusive. Soft X-ray absorption spectroscopy (XAS) is a powerful method for providing evidence of this type of phenomena [20,21].

In this research effort, we utilized electrochemical and spectroscopic techniques including the RRDE technique, HR-XPS, and soft XAS to explore the ORR performance and bulk structural and electronic properties of a novel carbon-supported bi-core CuFe−N$_x$/C electrocatalyst. For comparison purposes, single-core Cu−N$_x$/C and Fe−N$_x$/C electrocatalysts were synthesized and characterized separately using the same experimental procedures.

2. Experimental

2.1. Catalyst preparation

A detailed synthesis procedure can be found in a relevant patent [22]. Very briefly, Fe−N$_x$/C, Cu−N$_x$/C, and bi-core CuFe−N$_x$/C electrocatalysts were synthesized from iron and copper phthalocyanine (Pc)-based precursors on a Ketjen black EC-600 JD carbon black (Akzo Nobel) support. For synthesis of the Fe−N$_x$/C electrocatalyst, 20.0 g Ketjen black was dispersed in a 500 mL ethanol solution containing 5.0 g FePc using a sonicating probe for 30 min, followed by vigorous stirring for 24 h at room temperature. After solvent removal by rotary evaporation, the resulting solid mixture was transferred to a rotary quartz reactor, and then pyrolyzed under argon flow at 2.0 L min^{-1} at 450 °C for 1 h and then at 800 °C for 2 h. The final catalyst was obtained after cooling to room temperature under continuous argon flow, and then milled using a planetary ball mill at 200 rpm for 30 min. For the synthesis of Cu−N$_x$/C and CuFe−N$_x$/C electrocatalysts, 4.5 g CuPc and a mixture of 5.0 g FePc and 4.5 g CuPc were used as the respective transition-metal precursors in the above procedure. The compositions of the as-obtained catalysts are listed in Table 1. A commercial Pt/C (30%) catalyst was obtained from the BASF Fuel Cell Inc. and used for comparative studies. All other chemicals (analytical-grade) were purchased from Sigma−Aldrich.

2.2. Electrochemical characterization

Electrochemical measurements were conducted in a standard three-compartment electrochemical cell in 0.1M KOH solution maintained at room temperature (20–25 °C) using a RRDE setup from the Pine Instrument Company connected to an Autolab bipotentiostat (PGSTAT302N). Composite electrodes were prepared on a glassy carbon disk substrate (5.61 mm dia.) surrounded by a gold ring, obtained from the Pine Instrument Company. Before measurements, the RDE was first polished successively with 1, 0.3,

and 0.05-micron alumina slurry (Buehler, Lake Bluff, IL) and then cleaned with distilled water under sonication. The catalyst inks were prepared by using a mixed solution (1:1 wt%) of 2-propanol (HPLC grade, Alfa Aesar) and deionized water (Mega pure, Millipore) at a concentration of 1.84 mg ml^{-1} for non-noble metal catalysts and 1.23 mg ml^{-1} for Pt/C and then sonicating for >30 min to produce a uniform suspension. 10 µL of the catalyst ink was dispersed uniformly on the glassy carbon (GC) substrate and dried at room temperature. The total catalyst loading was determined to be 75 µg cm^{-2} for CuFe−N$_x$/C, Cu−N$_x$/C and Fe−N$_x$/C films, and 50 µg cm^{-2} for commercial Pt/C (30%, E-TEK). A home-designed reversible hydrogen electrode (RHE) was used as the reference electrode and prepared with the same 0.1 M KOH electrolyte. A Pt wire was taken as the counter electrode. For RRDE measurements, the ring potential was held at 1.3 V. Cyclic voltammograms and ORR polarization curves for the composite electrodes were recorded in Ar- and O$_2$-saturated 0.1 M KOH electrolytes, respectively.

2.3. Physical characterization

A JEOL (JEM-2010) microscope was used to obtain TEM images of the samples. A few droplets of an ultrasonically dispersed suspension of each sample in ethanol were placed on a support and dried under ambient conditions.

XRD patterns of the Cu−N$_x$/C, Fe−N$_x$/C, and CuFe−N$_x$/C catalysts were collected with a Rigaku Ultima III diffractometer, using a Bragg-Brentano geometry and Cu Kα radiation (λ = 1.5418 Å) over a scan range of 10−90° (2θ) at a scan rate of 0.2° min^{-1} and resolution of 0.02°.

HR-XPS characterization of the Cu−N$_x$/C, Fe−N$_x$/C, and CuFe−N$_x$/C catalysts, as well as iron and copper phthalocyanine compounds (Alfa Aesar), was performed using a Scienta ESCA 300
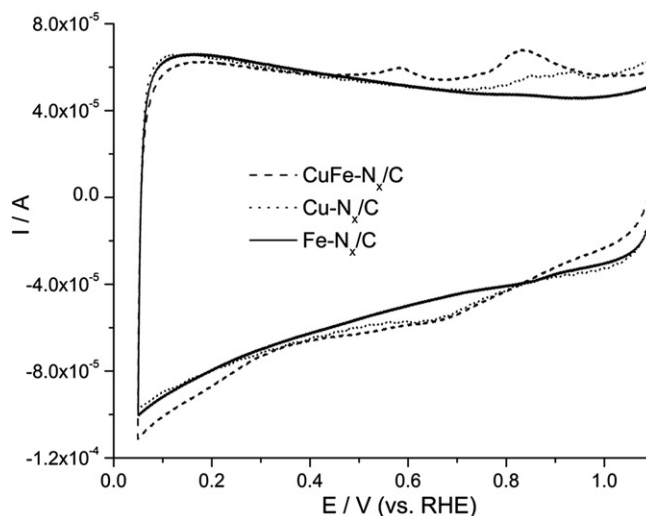

Fig. 1. Cyclic voltammograms of CuFe−N$_x$/C, Cu−N$_x$/C, and Fe−N$_x$/C catalysts in Ar-saturated 0.1 M KOH. Scan rate: 50 mV s^{-1}.
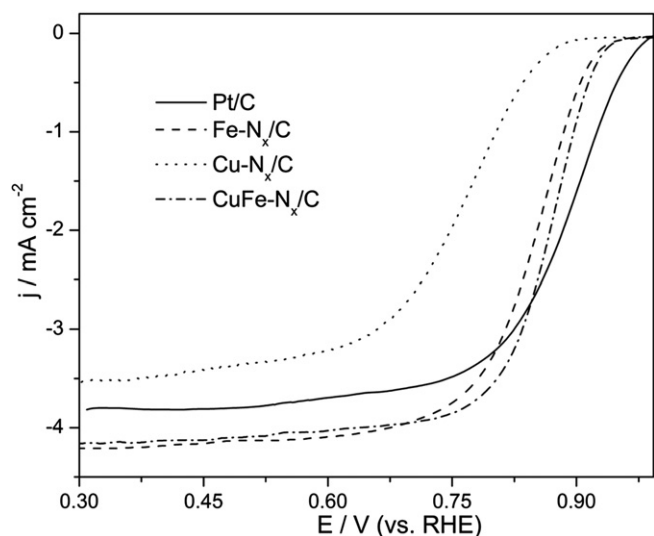
Fig. 2. RDE current density (based on the geometric area of the glassy carbon electrode) at 900 rpm in O_2-saturated 0.1M KOH on Cu–N_x/C, Fe–N_x/C, CuFe–N_x/C and commercial Pt/C (E-TEK, 30%) catalysts. Scan rate: 10 mV s^{-1}.

spectrometer, equipped with a monochromated Al Kα X-ray (hν = 1486.7 eV) source and enhanced signal detection instrumentation utilizing a 300-mm radius hemispherical analyzer and position-sensitive detector. All samples for HR-XPS

characterization were prepared in air by pressing powered material into conductive carbon tape. Spectra were obtained using a takeoff angle of 90° with respect to the surface plane of the sample. The analyzer pass energy was set at 150 eV, giving a resolution of the analyzer of 0.15 eV. All XPS spectra were calibrated against a value of the C1s binding energy (BE) of 284.5 eV for carbon black. Curve fitting for Cu2p and N1s spectra was accomplished by employing CASA XPS MFC application software (version 2.3.15). A Shirley background function and a Gaussian/Lorentzian (70/30) peak shape were selected for fitting the Cu2p and N1s peaks. The full-width-at-half-maximum (FWHM) of each component peak of Cu2p and N1s was set to 1.50 and 1.0 eV, respectively.

Synchrotron-based soft XAS experiments were carried out using undulator beamline 8.0.1 at the Advanced Light Source (ALS). The undulator and spherical grating monochromator supply a linearly polarized photon beam with resolving power up to 6000 [23]. Powder samples were spread onto a flat surface and loaded immediately into an ultrahigh vacuum chamber. Experiments were performed at room temperature and double checked at the low temperature of 80 K with linear polarization of the incident beam inclined 45° to the sample surfaces. Because the metallomacrocycle materials are well incorporated in carbon, we collected non-surface-sensitive XAS spectra by recording the total fluorescence yield (TFY). All data shown are normalized to the incident photon flux monitored by a clean gold mesh. The energy values of the spectra were calibrated by measuring reference samples of Fe and Cu metals. We have carefully checked and avoided any effects from
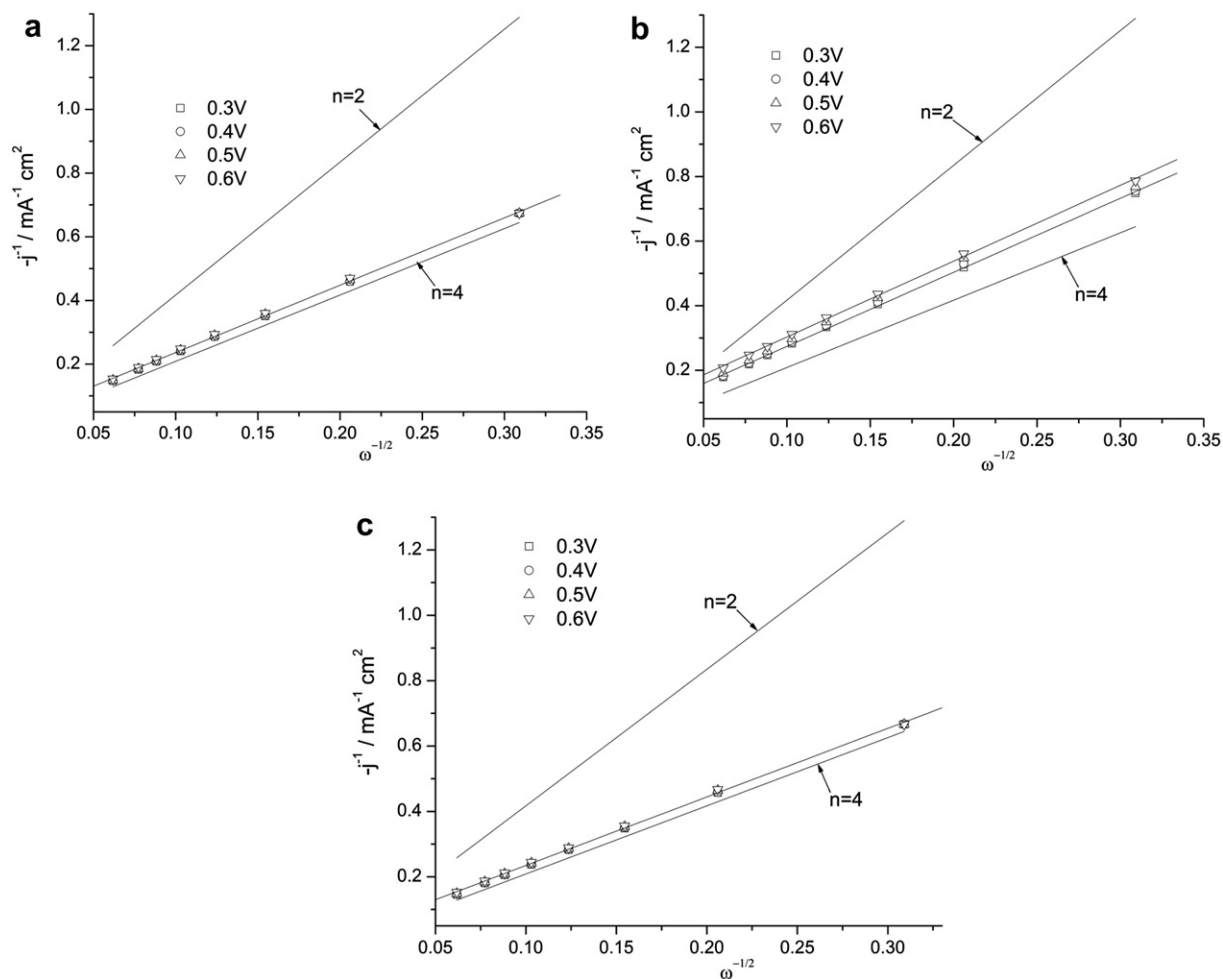

Fig. 3. Koutecky-Levich plots for ORR in O_2-saturated 0.1 M KOH solution at different potentials of (a) CuFe–N_x/C, (b) Cu–N_x/C, and (c) Fe–N_x/C.
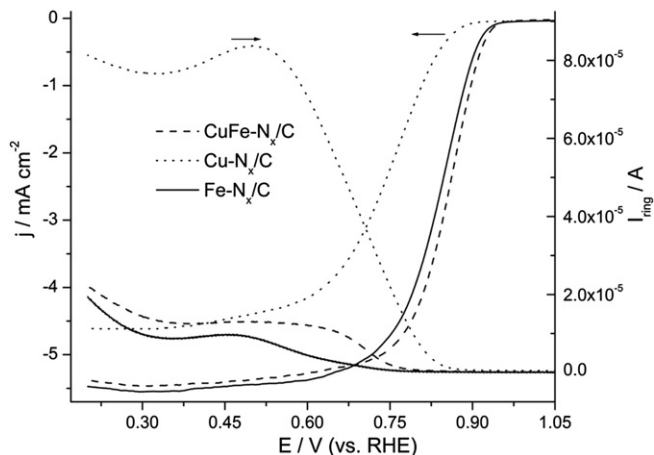
Fig. 4. RDE current density (based on the geometric area of the glassy carbon electrode) and ring current at 1600 rpm obtained in O_2-saturated 0.1M KOH on (a) CuFe−N_x/C, (b) Cu−N_x/C, and (c) Fe−N_x/C. Scan rate: 10 mV s^{-1}.

radiation damage during data collection. The overall resolution of XAS was better than 0.2 eV.

Transition-metal (TM) *L*-edge XAS provides a simple but direct probe of the excitations of *2p* core level electrons to the unoccupied *3d* states for *3d* transition-metals [20,21]. Because the *2p* core levels are featureless and narrow, the XAS lineshape provides abundant information on the electronic structure of the unoccupied *3d* states. In particular, the sensitivity to valence through TM-L edge measurements has been well established for Fe- and Cu-compounds [24,25].

3. Results and discussion

3.1. ORR electrocatalyst performance

Fig. 1 shows cyclic voltammograms of Cu−N_x/C, Fe−N_x/C, and CuFe−N_x/C electrodes in Ar-saturated 0.1M KOH. Large double-layer capacitance currents that originate from the underlying pyropolymer and supporting carbon matrix can be observed on all electrodes. The cyclic voltammogram of the Fe−N_x/C electrode is featureless, providing evidence that the coordination of Fe and the surrounded N atoms changed significantly after pyrolysis at high-temperature [26]. A catalytic site with molecular structure of C−Fe−N_x which is ill-defined on CVs, may have been formed [27]. In contrast, the first anodic peak around 0.58 V on the CuFe−N_x/C electrode may be ascribed to oxidation of Cu species. The absence of this peak on the Cu−N_x/C electrode in Fig. 1 indicates that electronic state and local environment of Cu atoms in Cu−N_x/C is very different from those in CuFe−N_x/C. Due to the same reason, the
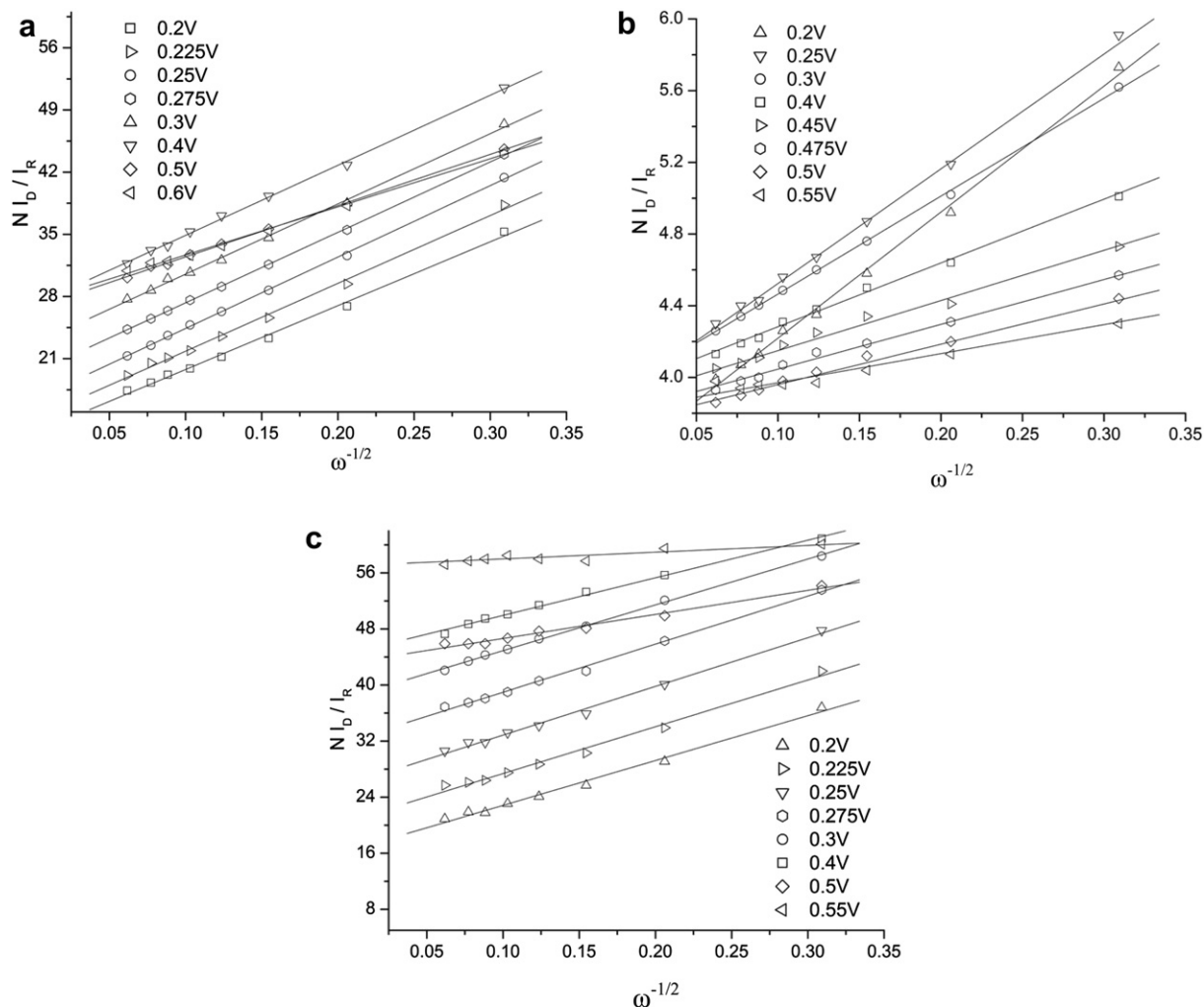

Fig. 5. NI_D/I_R vs. $\omega^{-1/2}$ plots for the ORR in O_2-saturated 0.1 M KOH solution at different potentials of (a) CuFe−N_x/C, (b) Cu−N_x/C and (c) Fe−N_x/C.
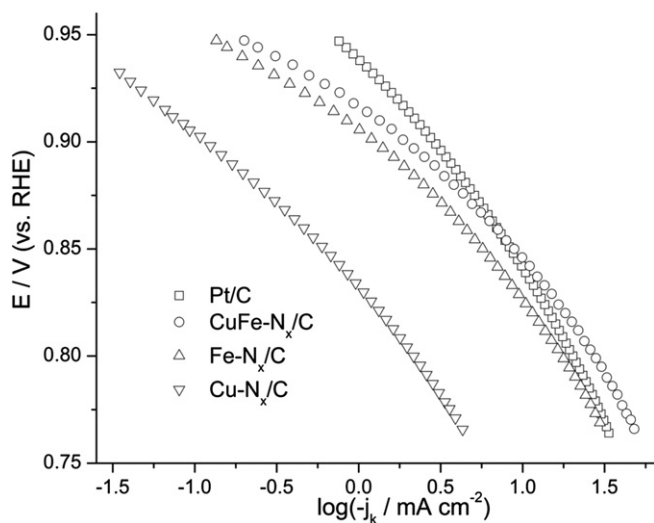
Fig. 6. Tafel plots for the ORR on Pt/C and CuFe−N$_x$/C, Cu−N$_x$/C, and Fe−N$_x$/C composite electrodes.

CuFe−N$_x$/C and Cu−N$_x$/C show successive anodic peaks with distinctive shape and position. However, the corresponding cathodic peaks for CuFe−N$_x$/C and Cu−N$_x$/C have similar position and intensity, indicating a similar amount of surface Cu species on both catalysts.

Fig. 2 shows RDE scans for the ORR in O$_2$-saturated 0.1 M KOH on the CuFe−N$_x$/C, Fe−N$_x$/C, Cu−N$_x$/C and Pt/C electrodes at 900 rpm. In all cases, three separate potential regions can be identified. For the CuFe−N$_x$/C, Fe−N$_x$/C and Pt/C electrodes, a mixed diffusion-kinetic limited region (0.65 V < E < 0.85 V) is sandwiched between a diffusion-controlled region (E < 0.65 V) and a Tafel region (E > 0.85 V). For the Cu−N$_x$/C electrode, the three regions shift negatively by 50 mV. The ORR current density j is expressed by Koutecky−Levich Eqs. (1) and Eq.(2) [28].

$$\frac{1}{j} = \frac{1}{j_k} + \frac{1}{j_d} \tag{1}$$

$$j_d = 0.620 nFD^{2/3} C_O \nu^{-1/6} \omega^{1/2} \tag{2}$$

where j_k is the kinetic current density, j_d is diffusion-limiting current density, n is the number of exchanged electrons, ω is the angular frequency of rotation, F is the Faraday constant (96,485 C mol^{-1}), D is the diffusion coefficient of molecular O$_2$ in

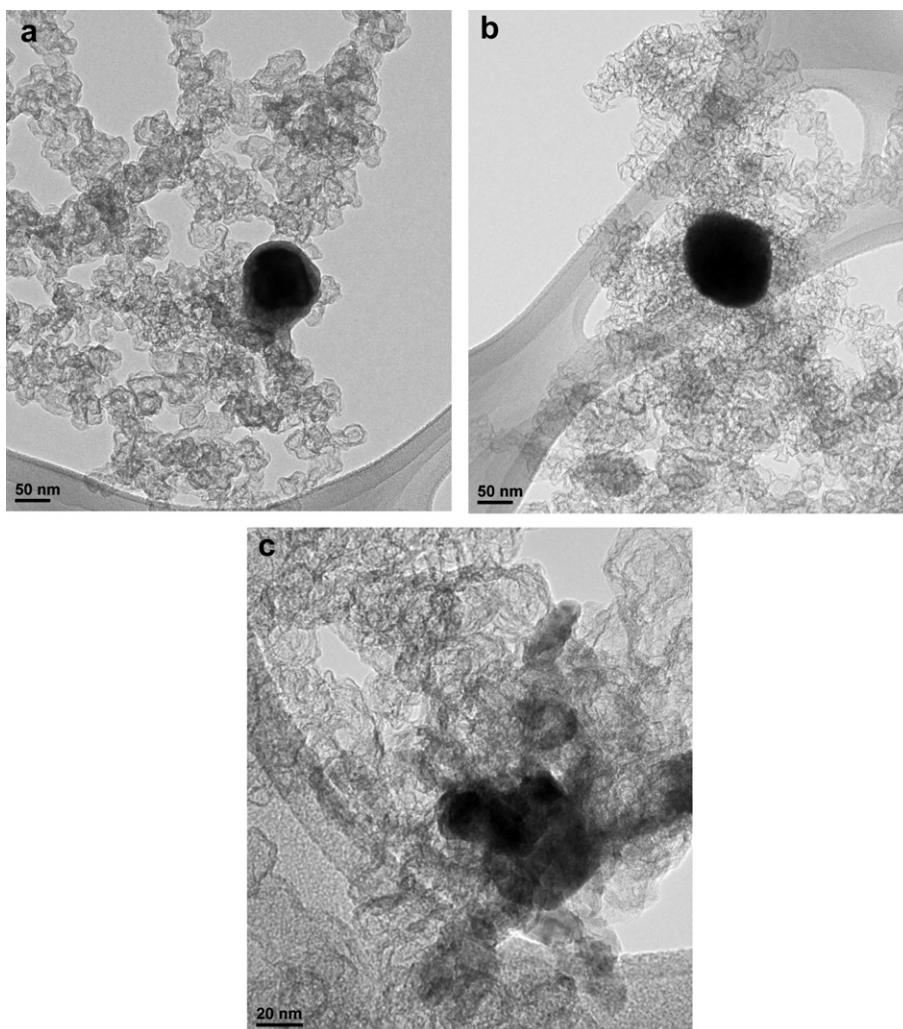**Fig. 7.** Transmission electron micrograph of (a) CuFe−N$_x$/C, (b) Cu−N$_x$/C and (c) Fe−N$_x$/C.

0.1 M KOH solution (1.9×10^{-5} cm^2 s^{-1}), ν is the kinematic viscosity (1×10^{-2} cm^2 s^{-1}), and C_O is the concentration of molecular oxygen (1.2×10^{-6} mol cm^{-3}) [29,30].

The $1/j$ vs. $1/\omega^{1/2}$ plots with data derived from ORR curves obtained at different rotation rates (not shown) on the CuFe−N$_x$/C, Fe−N$_x$/C and Cu−N$_x$/C electrodes are shown in Fig. 3a−c. Theoretical slopes for 2-electron and 4-electron ORR are shown in the same graphs. The numbers of exchanged electrons were calculated from the slopes of straight lines. The values of exchanged electrons n were determined from the slopes of the plots and listed in Table 1. The n values of various catalysts in Table 1 were illustrative of the 4-electron charge transfer pathway of the ORR process on both CuFe−N$_x$/C and Fe−N$_x$/C electrocatalysts. However, the calculated n value for Cu−N$_x$/C in 0.1M KOH is only 3.55, indicating the incomplete reduction of oxygen. The low n value for Cu−N$_x$/C may be due to the presence of metallic Cu because transition-metals tend to produce H$_2$O$_2$, an intermediate in oxygen reduction that cannot be further reduced to H$_2$O [31,32]. In support of this conclusion is our analysis of the XRD patterns in the following section.

The validity of the above Koutecky-Levich plots results was further examined by the RRDE experiments. With rotation of the electrode, any H$_2$O$_2$ (or O$_2$H$^-$) formed and desorbed at the disk electrode can be oxidized and monitored at the ring electrode potentiostated at 1.3 V (vs. RHE). Fig. 4 shows the ring current along with the disk current during the ORR on the CuFe−N$_x$/C, Fe−N$_x$/C, and Cu−N$_x$/C electrodes at 1600 rpm in 0.1M KOH. The relative amounts of H$_2$O$_2$ (or O$_2$H$^-$) formed on the catalysts at typical fuel cell operating potentials (0.6 V and 0.7 V) are given in Table 1, as based on the formula:

$$\chi_{H_2O_2} = \frac{2I_R/N}{I_D + I_R/N}$$

$$N = 0.31$$

(3)

where N is the collection efficiency of the ring, χ is the mole fraction of peroxide formed, and I_D and I_R are the disk and ring currents, respectively.

From Fig. 4, a significantly higher ring current and a lower disk current are seen on the Cu−N$_x$/C electrode, as compared to that on the CuFe−N$_x$/C and Fe−N$_x$/C electrodes. This result is consistent with the deviation from the 4-electron charge transfer pathway for the ORR process on the Cu−N$_x$/C electrocatalyst, as derived from the Koutecky-Levich plots in Fig. 3.

For another comparison of the intrinsic catalytic activity of as-synthesized Fe and Cu based non-noble metal catalysts toward the ORR, mass-transport-corrected Tafel plots were constructed. As a prerequisite, the reaction order (m) of the ORR on each catalyst must be obtained and verified. Although the m value can be calculated from the slope of plots of log(j) versus log($1−j/j_d$) indicated in equation (1) at different rotation rates and specific electrode potentials [33−35], a very sensitive criterion for first-order kinetics with respect to dissolved O$_2$ is a linear dependence of NI_D/I_R on $\omega^{-1/2}$ [36]. (The symbols have the same meanings as indicated in Eq.(3).) The linearity of NI_D/I_R vs. $\omega^{-1/2}$ plots in the potential range 0.2 V−0.6 V (vs.RHE) shown in Fig. 5a−c confirmed a first-order ORR for all three catalyst materials. As a result, Tafel curves can be derived according to the following equation [34,37]:

$$E = E_0 + b\log\frac{j_k}{j_0}$$

(4)

where E_0 is the equilibrium open-circuit potential ($E_0 = 1.229$ V vs. RHE under standard conditions), b is the Tafel slope, $j_k = j \cdot j_d/j_d − j$

is the kinetics current density, and j_0 is the exchange current density.

Fig. 6 shows the kinetic current densities j_k plotted as a function of the electrode potential (Tafel plots) for the CuFe−N$_x$/C, Fe−N$_x$/C, and Cu−N$_x$/C catalysts. As a frame of reference, the Tafel plot obtained on a commercial Pt/C catalyst (30%, BASF Fuel cell) for the ORR in 0.1M KOH is also presented in the same graph. The values of mass activity [38] of as-synthesized catalysts and commercial catalyst toward ORR were calculated at different potentials. As two important parameters to evaluate the intrinsic activity of catalyst materials for the ORR, the mass activity and half-wave potentials ($E_{1/2}$) obtained from the disk polarization curves in Fig. 4 are summarized in Table 1. Intriguingly, the Fe−N$_x$/C and CuFe−N$_x$/C catalysts show performance values comparable to those for Pt/C for the ORR in alkaline media. It is also interesting to note that Cu−N$_x$/C shows lower catalytic activity than Fe−N$_x$/C and a negative shift of $E_{1/2}$ as much as 89 mV due to incomplete reduction of oxygen. However, the capability to reduce oxygen is enhanced on CuFe−N$_x$/C as compared to Fe−N$_x$/C, even though the CuFe−N$_x$/C was synthesized using the same raw materials and procedure as for Cu−N$_x$/C and Fe−N$_x$/C. This result indicates that the adsorption of oxygen, desorption of reduction products, and electron transfer all become more facile upon the addition of Cu−N$_x$ species into the Fe−N$_x$/C catalyst. In spite of the general transition in the Tafel slope, two Tafel regions were roughly defined for the low-overpotential range ($E > 0.85$ V) and the high-overpotential range ($E < 0.85$ V), respectively. The dependence of Tafel slopes on the potential for ORR may be attributed to both "energetic effects" (Temkin, Langmuir adsorption) [39,40] and "blocking effects" (surface coverage of OH controlling O$_2$ adsorption) [41]. As can be seen in Table 1, the values obtained on Pt/C and Fe−N$_x$/C agree quite well with those reported in the literature under similar conditions [5]. The similarity of the Tafel slope value for CuFe−N$_x$/C and Fe−N$_x$/C is indicative of the same pathways for the ORR electrocatalysis. However, the intermediate adsorption on Cu−N$_x$/C may follow a different model, based on the deviation of Tafel slopes from those on
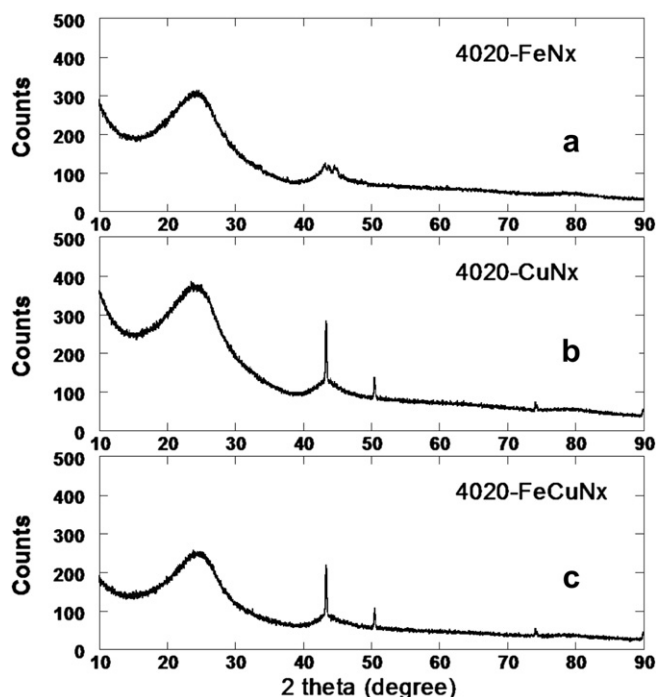

Fig. 8. X-ray diffraction patterns of CuFe−N$_x$/C, Cu−N$_x$/C, and Fe−N$_x$/C.

CuFe−N$_x$/C and Fe−N$_x$/C. Obviously, the active center for the ORR in the CuFe−N$_x$/C catalyst is still located on Fe. Meanwhile, the presence of Cu species may play an important role to accelerate charge transfer during the ORR process. Plausible mechanisms for this phenomenon are presented and discussed in Section 3.4.

3.2. Morphology and structural characterization

Fig. 7a−c show representative TEM images of the CuFe−N$_x$/C, Cu−N$_x$/C, and Fe−N$_x$/C electrocatalysts. General aspects of these three catalysts are similar, showing metal particles with sizes greater than 10 nm, and some of them (for CuFe−N$_x$/C and Cu−N$_x$/C) about 100 nm. These large particles are believed to be metallic Cu

or Fe formed during pyrolysis under Ar at high-temperature (800−900 °C). The size of the metallic particles for Fe−N$_x$/C is about one fifth of those for CuFe−N$_x$/C and Cu−N$_x$/C, which is consistent with the observation that the only a broad peak can be seen at ca. 43° in the XRD pattern of Fe−N$_x$/C as compared to the sharp peaks in the XRD patterns of Cu−N$_x$/C and CuFe−N$_x$/C (Fig. 8). The carbon particles of the support are clearly observed as large agglomerates, but the supported transition-metal composites (Fe−N$_x$, Cu−N$_x$, and CuFe−N$_x$) are not clearly distinguished in these images. This observation implies that the transition-metal composites are highly dispersed, and significant differences among these three electrocalaysts cannot be deduced by this technique. A deeper analysis of the TEM images suggests the presence of metal particles of a few
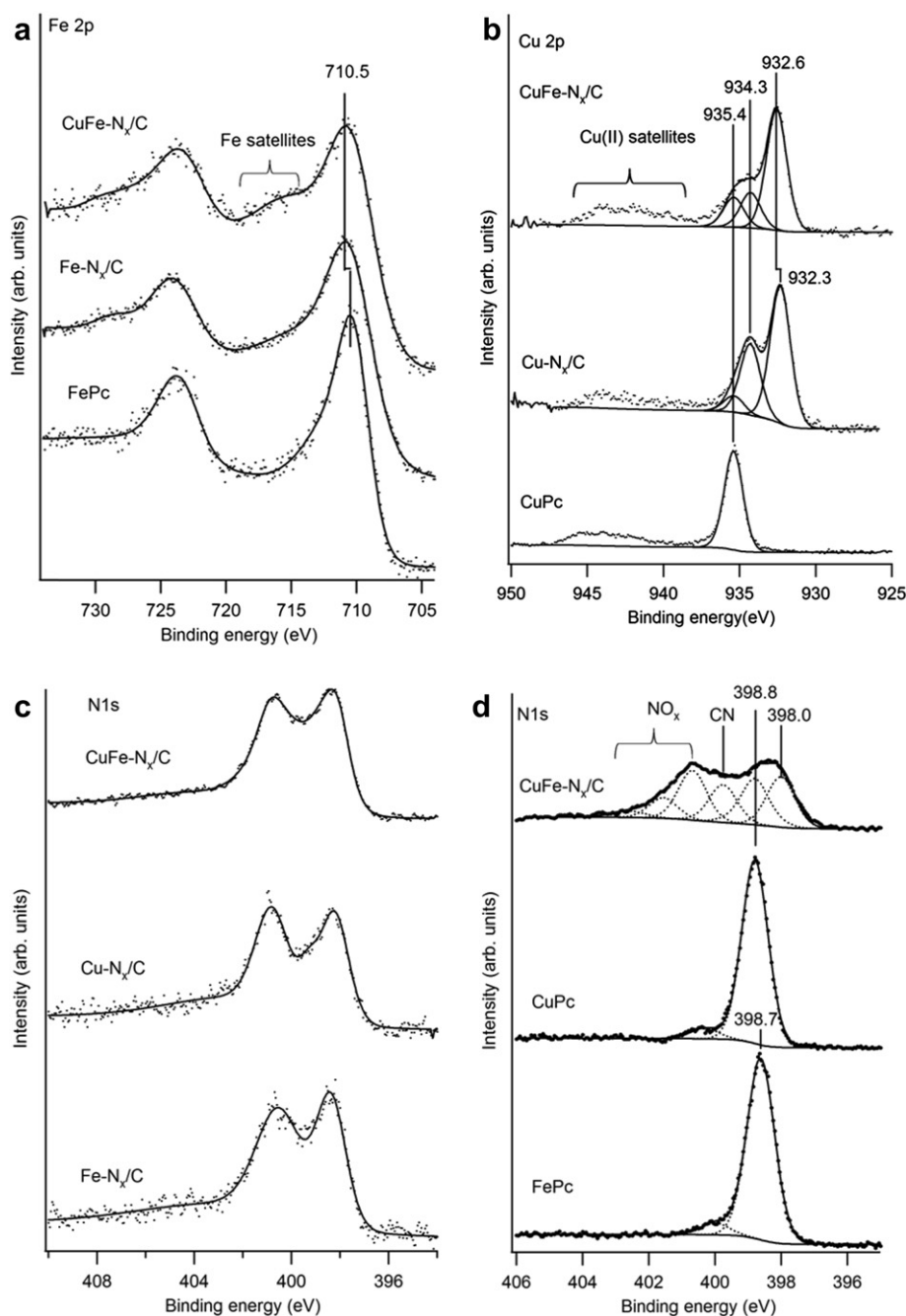

Fig. 9. (a) HR-XPS Fe2p spectra for Fe−N$_x$/C, CuFe−N$_x$/C and FePc, (b) HR-XPS Cu2p spectra for Cu−N$_x$/C, CuFe−N$_x$/C and CuPc, (c) HR-XPS N1s spectra for CuFe−N$_x$/C, FePc and CuPc, and (d) HR-XPS N1s spectra for Cu−N$_x$/C, Fe−N$_x$/C and CuFe−N$_x$/C.

nanometers, or even sub-nanometric size, but precise identification of such particles is limited by the microscope resolution.

XRD patterns of the CuFe−N_x/C, Cu−N_x/C, and Fe−N_x/C composite catalysts are shown in Fig. 8. The broad peaks at ca. 24° are attributed to disordered graphite (002) diffraction of the carbon support in all three spectra. The absence of sharp peaks in the XRD pattern of Fe−N_x/C (Fig. 8a) indicates that there is no magnetite formation during the high-temperature pyrolysis [42]. In contrast, the sharp peaks in Fig. 8b and 8c indicate that there was metallic Cu (Fm3m, cubic) formation in Cu−N_x/C and CuFe−N_x/C. This metallic Cu has no activity for the ORR, and its presence may be one of the causes of the lower values of exchanged electrons (n) for the Cu−N_x/C catalyst during the ORR shown in Table 1.

3.3. HR-XPS study

HR-XPS spectra of all samples are displayed in Fig. 9, showing scans of the Fe2p, Cu2p, and N1s regions. Compared to the Fe2p peak of FePc/C, the high-temperature annealed samples show broadened Fe2p main peaks at slightly higher binding energy (BE) and increased intensity of satellite features in the region near 716 eV BE as shown in Fig. 9a. The Fe2p main peak of Fe−N_x/C is at the same BE as in Cu−Fe−N_x/C samples, but the satellite intensity is larger for CuFe−N_x/C. This shows that some Fe species in CuFe−N_x/C are in a different electronic environment from that of Fe−N_x/C, but a clear assignment of the Fe oxidation state cannot be made on this basis alone. The companion $Cu2p_{3/2}$ peaks are displayed in Fig. 9b. $Cu2p_{3/2}$ spectra of CuPc/C before annealing are characterized by the presence of a narrow main peak at 935.4 eV BE and a broad Cu(II) satellite feature extending from 940 to 947 eV BE. After annealing, large changes in the Cu2p spectra were observed. The region near the $Cu2p_{3/2}$ main peak can be deconvoluted into three components at 935.4, 934.3 and either 932.3 eV BE for Cu−N_x/C or 932.6 eV BE for CuFe−N_x/C. The small $Cu2p_{3/2}$ peak at 935.4 eV BE could be due to a small amount of undecomposed CuPc or formation of Cu(II) hydroxide from air exposure. The appearance of $Cu2p_{3/2}$ peaks at lower BEs, at 934.3 and 932.6 eV BE must arise from reduction to Cu(I) due to decomposition/deligandation of during high-temperature treatment, The decrease in the Cu(II) satellite intensity is consistent with this reduction. The spectra for Cu−N_x/C and CuFe−N_x/C are similar. However, the Cu(I)$2p_{3/2}$ peak in CuFe−N_x/C was at 932.6 compared to 932.3 eV BE of Cu−N_x/C, the intensities of the peaks at 935.4 and 934.3 eV BE are altered, and the satellite intensity for CuFe−N_x/C was increased. These changes indicate an altered environment for Cu by the presence of Fe species in CuFe−N_x/C compared to Cu−N_x/C.

All of the catalysts have similar N1s spectra, as shown in Fig. 9c. This indicates that the heat treatment used in catalyst preparation caused a similar "C−N_x" structure in all three catalyst samples. The N1s spectra for FePc, CuPc, and CuFe−N_x/C are compared in Fig. 9d. FePc and CuPc are characterized by a single peak at 398.7 and 398.8 eV BE, respectively. The small peak at about 400 eV BE is due to contamination or oxidation from air exposure. The N1s spectrum for the CuFe−N_x/C catalyst is very broad and shows the presence of multiple nitrogen species (five peaks are used to simulate the spectra). Peaks at 400 eV or higher BE are caused by oxidation that results in NO_x species. The peak at 400 eV BE is assigned to C=N and C≡N species. The presence of lower BE peaks at 398.8 and 398.0 eV are assigned to N atoms directly bonding to Fe and/or Cu in the catalyst.

In summary, the HR-XPS analysis shows that the high-temperature catalyst preparation process caused extensive but incomplete decomposition of the FePc and CuPc precursors and the resulting catalysts retain substantial metal-N bonding forming reduced nitrogen species. HR-XPS shows differences in the charge

states and distribution of oxidation states of both metals in the bi-core CuFe−N_x/C catalyst compared to the Cu−N_x/C and Fe−N_x/C catalysts. However, a clearer view of the nature of these changes comes from XAS studies, discussed below.

3.4. XAS spectroscopic study

Typically, soft x-ray XAS of the $3d$ TM-L edges represents absorption transitions from the $2p^63d^n$ to the $2p^53d^{n+1}$ electronic states. The spin−orbit interaction splits the 2p states into $2p_{1/2}$ and $2p_{3/2}$, leading to two groups of well-separated peaks, *i.e.*, high energy L_2 and low-energy L_3 peaks. This is evident in both the Fe-$L_{2,3}$ and Cu-$L_{2,3}$ spectra in Fig. 10a and b. Here we focus on the lineshapes of the L_3 peaks of Fe- and Cu- spectra, which are very sensitive to the change of the crystal fields and valence of the $3d$ elements [20,24].

As shown in Fig. 10a, the Fe L edge XAS spectra of Fe−N_x/C and CuFe−N_x/C are very different. Two features in the L3 peak around 707 eV, corresponding to major crystal field splitting, are marked as A and B. The change of the intensity ratio of these two peaks clearly shows the change of the Fe valence in the samples [20,24]. The much higher intensity of the B state indicates that the Fe valence evolves from 2+ toward 3+ for Fe−N_x/C and CuFe−N_x/C, respectively. A qualitative difference of the $L3$ XAS lineshape is also evident in Cu-L edge spectra around 935 eV, as shown in Fig. 10b. The weakening of the L3 leading peak at about 933 eV for CuFe−N_x/C is the fingerprint of Cu valence changing from +2 for Cu−N_x/C to +1 for CuFe−N_x/C [43].

The aforementioned variation of the TM-L edge XAS data provides direct evidence for the existence of significant interaction between Fe and Cu in CuFe−N_x/C. Otherwise, if CuFe−N_x/C was present only as a simple physical mixture of Cu−N_x/C and Fe−N_x/C,
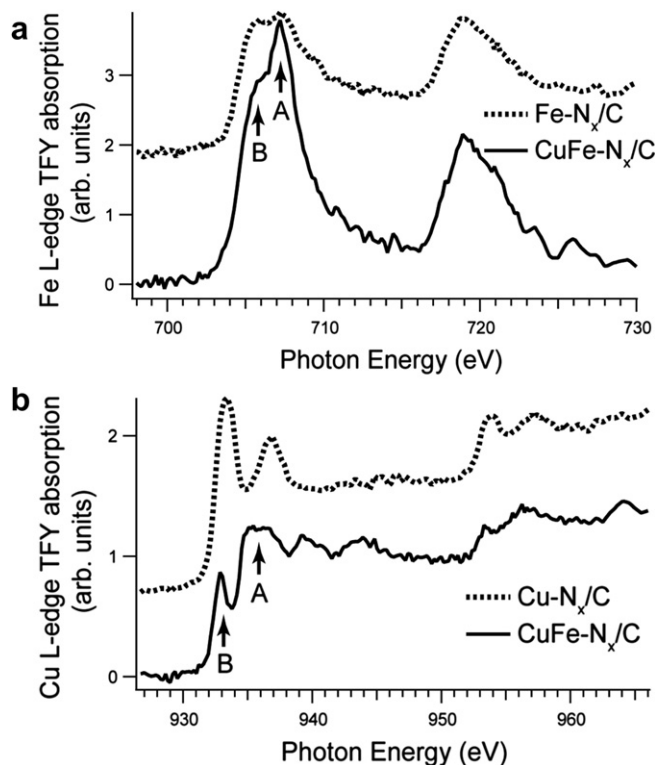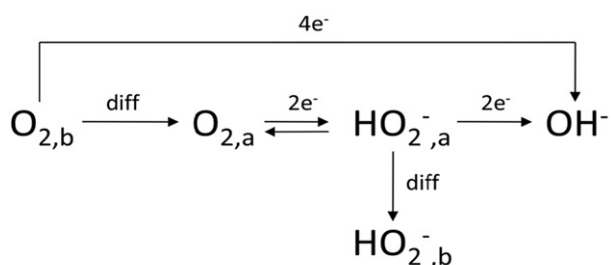

Fig. 10. (a) Fe L edge TFY spectra of Fe−N_x/C and CuFe−N_x/C (vertically offset for clarity), (b) Cu L edge TFY spectra of Cu−N_x/C and CuFe−N_x/C (vertically offset for clarity).

$$4e^-$$

$$O_{2,b} \xrightarrow{\text{diff}} O_{2,a} \xrightleftharpoons{} HO_2^-{}_{,a} \xrightarrow{2e^-} OH^-$$

diff

$$HO_2^-{}_{,b}$$

b: bulk, a: adsorption; diff: diffusion

Fig. 11. General scheme of oxygen reduction in alkaline media.

one would expect the bi-core L edge XAS spectra for Cu and Fe to be identical to those for single-core Cu and Fe. The valence change from 2+ to 3+ for Fe, along with 2+ to 1+ for Cu, indicates that this interaction results in charge transfer between the Fe and Cu transition-metal centers. It should be emphasized that charge transfer from the Fe center to the Cu center may involve, on average,

a fraction of an electron rather than a full electron. However, even a small valence change could greatly boost the Cu reducing power, presumably more significantly than the diminishing Fe reducing power. This scenario, based on clear XAS evidence, provides important insight to understand the increased ORR performance of CuFe−N_x/C compared with Fe−N_x/C.

3.5. ORR mechanism discussion

There remains some uncertainty about the active sites of metal-N_4 chelates catalysts adsorbed on carbon after heat treatment. Van Veen et al. suggested that the catalytic site of macrocycle catalysts is the Me-N4 moiety at all pyrolysis temperatures [7,9,11]. On the contrary, Yeager et al. claimed that the catalytic activity of heat-treated macrocycle catalysts for the ORR is attributed to a C−N_x−Me complex [8,44]. However, they contend that the C−N_x−Me complex is not formed during, but rather after, pyrolysis. Pyrolysis at high-temperature leads to formation of metal oxide phases which dissolve into the acidic electrolyte and subsequently readsorb on the C−N_x functional groups. In addition, other authors
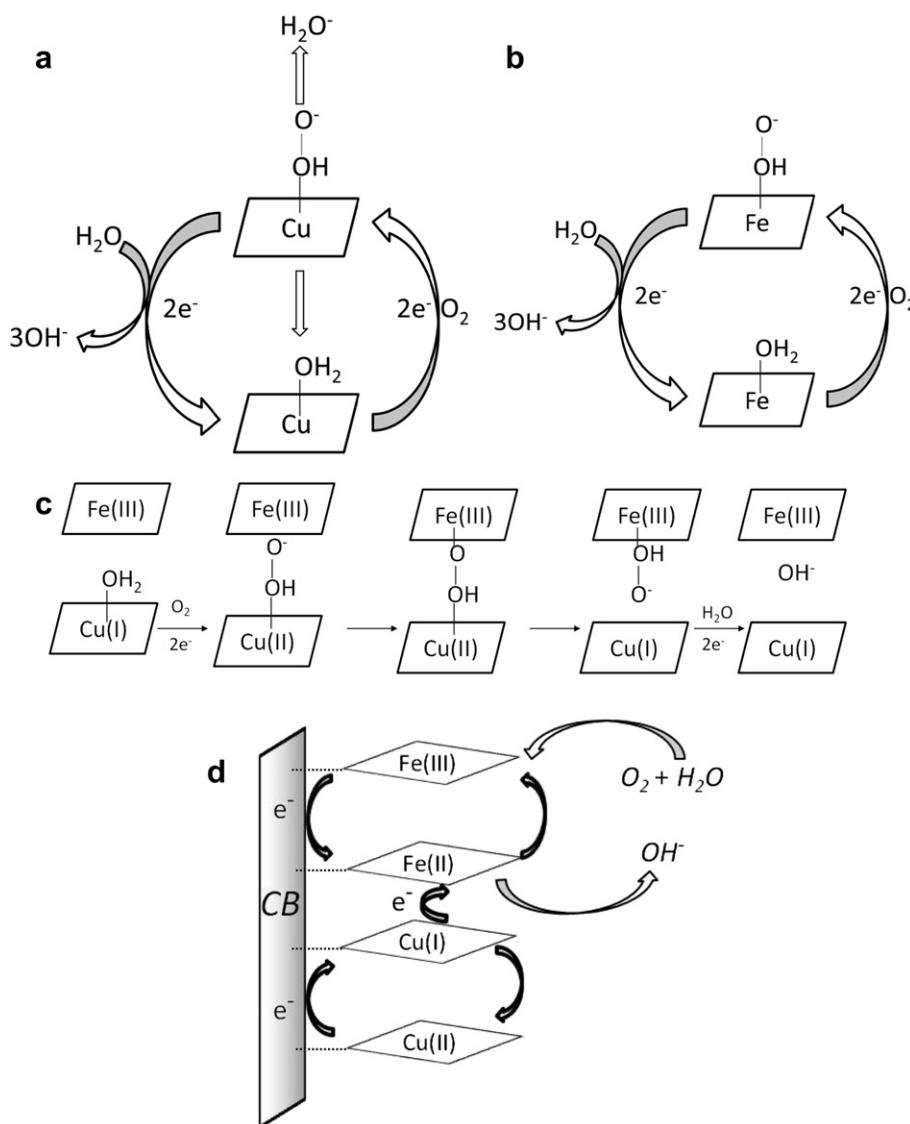

Fig. 12. Diagrams of operating mechanism for the ORR on (a) Cu−N_x/C catalyst, (b) Fe−N_x/C catalyst, (c) CuFe−N_x/C catalyst assuming the Cu(I) is the first site for O_2 adsorption, and (d) CuFe−N_x/C catalyst assuming the Fe(III) is the site for O_2 adsorption.

proposed that the activate sites involve only a special form of carbon with nitrogen functional groups. The metal ions in the Me−N$_4$ chelates are useful only to promote decomposition of the chelate upon thermal treatment [6,45]. Although these conclusions are likely to be true under specific preparation conditions (type of carbon, precursors of N and metal, reaction time, temperature, and purging gas of the thermal treatment), we are inclined to believe that a composite material containing both active sites (C−N$_x$−Metal) and inactive components (metallic clusters, metal oxides) can be formed during the high-temperature heat treatment in our cases. Two observations support this conclusion. First, from the HR-XPS results shown in Fig. 9, the "C−N$_x$" structure is similar in all of the catalysts. If C−N$_x$ moieties are the most active sites for the ORR, then the performance of Cu−N$_x$/C should be close to that of Fe−N$_x$/C. However, from Fig. 6 the kinetic current for the ORR on Cu−N$_x$/C is an order of magnitude lower than that on Fe−N$_x$/C at 0.85 V (vs. RHE). This result indicates that the metal plays an important role in the electroreduction of oxygen. Secondly, from our efforts to obtain a catalyst with a higher metal loading, excess metal oxide was formed and there was no improvement in the ORR rate. This implies that the maximum number of active centers, consisting of metal centers stabilized by nitrogen-containing ligands, is limited by the total surface area of the supporting materials where the ligands must exist. In conclusion, the coordination of the metal with nitrogen is a necessary condition for the macrocycle catalysts to show good ORR performance.

Oxygen reduction in an alkaline medium appears to occur according to the general scheme shown in Fig. 11. The presence of Cu−N$_x$/C, Fe−N$_x$/C, or CuFe−N$_x$/C catalyst helps to lower the activation energy in physical steps such as electron transfer and chemical steps such as adsorption of reactants, desorption of products, and disproportionation of intermediates. Upon O$_2$ approach to the catalyst surface, there is interaction of the O$_2$ π orbitals with the partially filled d orbitals of either Cu or Fe. [46]. Fig. 4 shows that the onset potential for the ORR on Cu−N$_x$/C is 90 mV more negative than that on Fe−N$_x$/C. This potential difference can be explained by the fact that the FePc system has significant d orbital character near the Fermi energy, whereas occupied and unoccupied d orbitals of the CuPc system lie more than 1 eV from the Fermi energy [47−49]. Assuming that a water molecule is coordinated to the active sites of the catalyst in the absence of O$_2$, pathways for the ORR on Cu−N$_x$/C and Fe−N$_x$/C can be postulated as shown in Fig. 12a and b. Fig. 12a and b are distinguished by whether the adduct of the catalyst with O$_2$ is decomposable during the ORR process. The mechanism of the ORR on Fe−N$_x$/C is consistent with Anderson's conclusion for the intermediate steps of ORR on Fe-ion-coordinated N$_4$ chelates [50]. In their quantum theory study, they confirmed that the Fe-(OHOH) bond is strong enough to prevent H$_2$O$_2$ from releasing as a two-electron reduction product. Also, they ascribe this stable intermediate to the strong hydrogen bonding between −(OHOH) and the lone-pair orbitals belonging to N$_x$.

The increased catalytic activity by forming a binary CuFe−N$_x$/C rather than Fe−N$_x$/C or Cu−N$_x$/C is likely caused by the decrease in the activation energy of the ORR. To elucidate which step (adsorption of reactants, electron transfer, bond formation and breakage, desorption of products, etc.) requires further quantum studies and DFT calculations. Nevertheless, as discussed in the above section, XAS data reveal the variation of Fe and Cu electronic states toward respective higher and lower valence states when forming the CuFe−N$_x$/C, thereby demonstrating the interaction between the two metal centers to promote effective charge transfer. Consequently, plausible working mechanisms of the ORR on the CuFe−N$_x$/C catalyst can be proposed, and they are illustrated in Fig. 12c and d. In the first scenario, the Cu(I) is favored over Fe(III) in

the first step of O$_2$ adsorption due to the strong bonding of H$_2$O to the Fe(III) site. As a result, the oxygen is reduced to an intermediate species followed by transfer to the Fe(III) site for further reduction to water. Generally, the Cu(I) site is more active in the first two-electron transfer, and the Fe(III) site is more efficient for the last two-electron transfer during the overall ORR process. In contrast, the second scenario shows a redox-mediated mechanism. Basically, this reaction mechanism may involve a combined effect of Fe and Cu wherein N$_x$Fe(III) serves as the ORR active site and Cu(I)/Cu(II) serves as the redox mediator during the ORR. Reminiscent of the role of the redox mediator of Ru(NH$_3$)$_6^{2+}$/Ru(NH$_3$)$_6^{3+}$ for the ORR on cobalt(II) tetrakis(4-N-methylpyridy1)porphyrin, the Cu(II)/Cu(I) redox mediator may help to transport electrons from the electrode to the catalyst sites and thereby accelerate the reduction of the adduct of N$_x$FeO$_y$H$_z$.

4. Conclusions

Three non-noble metal catalysts, Cu−N$_x$/C, Fe−N$_x$/C, and CuFe−N$_x$/C, were prepared by impregnation of iron and copper phthalocyanines or the mixture of these two precursors followed by a heat treatment at 800 °C under an Ar atmosphere. The as-synthesized materials contain single metal ions or double metal ions bonded to nitrogen atoms. From RRDE characterization, the Cu−N$_x$/C catalyst showed lower catalytic activity for the ORR with a 89 mV negative shift of $E_{1/2}$ and 10% of the kinetic current density at 0.85 V (vs. RHE), as compared to the Fe−N$_x$/C catalyst. However, it is interesting to find that the ORR performance of the bi-core CuFe−N$_x$/C catalyst was enhanced by the presence of Cu. The kinetic current density of this CuFe−N$_x$/C material was even higher than a commercial Pt/C catalyst at 0.85 and 0.80 V (vs. RHE). HR-XPS analysis provides evidence that the bonding between metal (Fe and Cu) and nitrogen is still maintained in the catalysts even after pyrolysis and the oxidation states of Fe and Cu are perturbed by the presence of the second metal component in the bi-core catalyst. Based on XAS results obtained on the Cu L edge and the Fe L edge, we determined that the bi-core CuFe−N$_x$/C catalyst exhibits additional reduced Cu ions and more oxidized Fe ions as compared to the "single-core" Fe−N$_x$/C. This characteristic may result in lower activation energy of the ORR. Although further quantum studies and DFT calculations are needed, two plausible scenarios for the mechanisms of the ORR on CuFe−N$_x$/C were proposed. In the first mechanism one step involves the adsorption of O$_2$ on Cu(I) and a second step involves the transfer of an O intermediate to Fe(III), followed by reduction of H$_2$O. In the second mechanism, the Cu(I)/Cu(II) serves only as a redox mediator to expedite electron transfer during the ORR at the Fe(II)/Fe(III) active center.

References

[1] J.R. Varcoe, R.C.T. Slade, Fuel Cells 5 (2005) 187−200.
[2] R.C.T. Slade, J.R. Varcoe, Solid State Ionics 176 (2005) 585−597.
[3] T.S. Olson, S. Pylypenko, P. Atanassov, K. Asazawa, K. Yamada, H. Tanaka, J. Phys. Chem. C 114 (2010) 5049−5059.
[4] Y. Wang, D. Zhang, H. Liu, J. Power Sources 195 (2010) 3135−3139.
[5] H.L. Pang, J.P. Lu, J.H. Chen, C.T. Huang, B. Liu, X.H. Zhang, Electrochim. Acta 54 (2009) 2610−2615.

[6] K. Wiesener, Electrochim. Acta 31 (1986) 1073–1078.
[7] J.A.R. Van Veen, H.A. Colijn, J.F. Van Baar, Electrochim. Acta 33 (1988) 801–804.
[8] D.A. Scherson, S.L. Gupta, C. Fierro, E.B. Yeager, M.E. Kordesch, J. Eldridge, R.W. Hoffman, J. Blue, Electrochim. Acta 28 (1983) 1205–1209.
[9] J.A.R. Van Veen, J.F. Van Baar, K.J. Kroese, J. Chem. Soc. Faraday Trans. 1 (77) (1981) 2827–2843.
[10] P. Vasudevan, Santosh, N. Mann, S. Tyagi, Transit. Met. Chem. (London) 15 (1990) 81–90.
[11] A.L. Bouwkamp-Wijnoltz, W. Visscher, J.A.R. van Veen, E. Boellaard, A.M. van der Kraan, S.C. Tang, J. Phys. Chem. B 106 (2002) 12993–13001.
[12] M. Lefevre, J.P. Dodelet, P. Bertrand, J. Phys. Chem. B 106 (2002) 8705–8713.
[13] A. Biloul, O. Contamin, G. Scarbeck, M. Savy, B. Palys, J. Riga, J. Verbist, J. Electroanal. Chem. 365 (1994) 239–246.
[14] A. Biloul, O. Contamin, M. Savy, G. Scarbeck, J. Riga, J. Verbist, J. Electroanal. Chem. 379 (1994) 321–328.
[15] J.P. Collman, N.K. Devaraj, R.A. Decreau, Y. Yang, Y.-L. Yan, W. Ebina, T.A. Eberspacher, C.E.D. Chidsey, Science 315 (2007) 1565–1568 (Washington, DC, U. S.).
[16] X. Li, G. Liu, B.N. Popov, J. Power Sources 195 (2010) 6373–6378.
[17] S. Li, L. Zhang, J. Kim, M. Pan, Z. Shi, J. Zhang, Electrochim. Acta 55 (2010) 7346–7353.
[18] A. Biloul, F. Coowar, O. Contamin, G. Scarbeck, M. Savy, D. van den Ham, J. Riga, J.J. Verbist, J. Electroanal. Chem. 350 (1993) 189–204.
[19] D. Chu, R. Jiang, Solid State Ionics 148 (2002) 591–599.
[20] F.d. Groot, A. Kotani, Core Level Spectroscopy of Solids, CRC Press, 2008.
[21] J. Stohr, NEXAFS Spectroscopy, Springer, 1996.
[22] S. Catanorchi, M. Piana. In: (Acta S.p.A., Italy). Application: WO, Chemical Indexing Equivalent to 151:452785 (EP) (2009) pp. 31.
[23] J.J. Jia, T.A. Callcott, J. Yurkas, A.W. Ellis, F.J. Himpsel, M.G. Samant, et al., Rev. Scientific Instruments 66 (1995) 1394–1397.
[24] P.L. Cook, X. Liu, W. Yang, F.J. Himpsel, J. Chem. Phys. 131 (2009) 194701/ 194701–194701/194710.
[25] J.P. Crocombette, M. Pollak, F. Jollet, N. Thromat, M. Gautier-Soyer, Phys. Rev. B: Condensed Matter 52 (1995) 3143–3150.
[26] R. Baker, D.P. Wilkinson, J. Zhang, Electrochim. Acta 54 (2009) 3098–3102.
[27] I.T. Bae, D.A. Tryk, D.A. Scherson, J. Phys. Chem. B 102 (1998) 4114–4117.
[28] E. Higuchi, H. Uchida, M. Watanabe, J. Electroanal. Chem. 583 (2005) 69–76.
[29] R.E. Davis, G.L. Horvath, C.W. Tobias, Electrochim. Acta 12 (1967) 287–297.
[30] K. Vaik, A. Sarapuu, K. Tammeveski, F. Mirkhalaf, D.J. Schiffrin, J. Electroanal. Chem. 564 (2004) 159–166.
[31] E.M. Crabb, R. Marshall, D. Thompsett, J. Electrochem. Soc. 147 (2000) 4440.
[32] U.A. Paulus, A. Wokaun, G.G. Scherer, T.J. Schmidt, V. Stamenkovic, N.M. Markovic, P.N. Ross, Electrochim. Acta 47 (2002) 3787–3798.
[33] C.-C. Chang, T.-C. Wen, H.-J. Tien, Electrochim. Acta 42 (1996) 557–565.
[34] Q. He, S. Mukerjee, R. Zeis, S. Parres-Esclapez, M.J. Illan-Gomez, A. Bueno-Lopez, Appl. Catal. A 381 (2010) 54–65.
[35] M.H. Lee, J.S. Do, J. Power Sources 188 (2009) 353–358.
[36] N.A. Anastasijevic, V. Vesovic, R.R. Adzic, J. Electroanal. Chem. Interfacial Electrochem. 229 (1987) 317–325.
[37] S. Baranton, C. Coutanceau, C. Roux, F. Hahn, J.M. Leger, J. Electroanal. Chem. 577 (2005) 223–234.
[38] E. Antolini, J.R.C. Salgado, M.J. Giz, E.R. Gonzalez, Int. J. Hydrogen Energy 30 (2005) 1213–1220.
[39] F.H.B. Lima, M.J. Giz, E.A. Ticianelli, J. Braz. Chem. Soc. 16 (2005) 328–336.
[40] M.T. Giacomini, E.A. Ticianelli, J. McBreen, M. Balasubramanianb, J. Electrochem. Soc. 148 (2001) A323–A329.
[41] N.M. Markovic, T.J. Schmidt, V. Stamenkovic, P.N. Ross, Fuel Cells 1 (2001) 105–116.
[42] V. Bambagioni, C. Bianchini, J. Filippi, A. Lavacchi, W. Oberhauser, A. Marchionni, S. Moneti, F. Vizza, R. Psaro, V. Dal Santo, A. Gallo, S. Recchia, L. Sordelli, J. Power Sources 196 (2011) 2519–2529.
[43] C.L. Chen, K.W. Yeh, D.J. Huang, F.C. Hsu, Y.C. Lee, S.W. Huang, G.Y. Guo, H.J. Lin, S.M. Rao, M.K. Wu, Phys. Rev. B: Condensed Matter Mater. Phys. 78 (2008) 214105/214101–214105/214105.
[44] A. Tanaka, S.L. Gupta, D. Tryk, C. Fierro, E.B. Yeager, D.A. Scherson, Proc. Electrochem. Soc. 92-11 (1992) 555–572.
[45] R. Franke, D. Ohms, K. Wiesener, J. Electroanal. Chem. Interfacial Electrochem. 260 (1989) 63–73.
[46] J.H. Zagal, Coord. Chem. Rev. 119 (1992) 89–136.
[47] X. Lu, K.W. Hipps, J. Phys. Chem. B 101 (1997) 5391–5396.
[48] U. Mazur, K.W. Hipps, J. Phys. Chem. 99 (1995) 6684–6688.
[49] U. Mazur, K.W. Hipps, J. Phys. Chem. 98 (1994) 8169–8172.
[50] A.B. Anderson, R.A. Sidik, J. Phys. Chem. B 108 (2004) 5031–5035.